



Focussed on "Crack Paths"



Influence of secondary dendrite arm spacing (SDAS) on the fatigue properties of different conventional automotive aluminum cast alloys

Sascha Gerbe, Ulrich Krupp

RWTH Aachen University, Steel Institute

Intzestr. 1, 52072 Aachen, Germany

sascha.gerbe@iehk.rwth-aachen.de, krupp@iehk.rwth-aachen.de

Wilhelm Michels

University of Applied Sciences Osnabrück, Institute of Materials Design and Structural Integrity

Albrechtstr. 30, 49076 Osnabrück, Germany

w.michels@hs-osnabrueck.de

ABSTRACT. For industrial in-series castings, the presence of casting defects, like porosity, geometrically complex intermetallic precipitates and the occurrence of eutectic silicon of varying morphologies, is well known but hard to prevent due to technical and economic limitations. To improve the performance and safety of cast aluminum products, the present work deals with the correlation between the cooling-rate-dependent secondary dendrite arm spacing (SDAS), the high- and very-high-cycle-fatigue (VHCF) behavior, the crack propagation mechanisms under pure bending with a focus on the crack propagation paths for near-threshold stress intensity factor ranges ΔK_I using two conventional automotive cast aluminum alloys AlSi8Cu3 (engine blocks) and AlSi7Cu0.5Mg (cylinder heads). Furthermore, the role of a variation in porosity on the crack initiation process is discussed. Specimens were extracted from in-series castings choosing positions with a maximal difference in cooling rate and SDAS, respectively. It is shown that porosity is highly influencing the crack initiation mechanism and that the SDAS has a strong influence on both, crack propagation rate and crack propagation paths. Hence, analogies between the SDAS and the grain size as influence factor according to the Hall-Petch relationship were identified.

KEYWORDS. Cast; Aluminum; SDAS; Threshold; Kitagawa-Takahashi-diagram; Hall-Petch relationship.



Citation: Gerbe, S., Krupp, U., Michels, W., Influence of secondary dendrite arm spacing (SDAS) on the fatigue properties of different conventional automotive aluminum cast alloys, *Frattura ed Integrità Strutturale*, 48 (2019) 105-115.

Received: 30.11.2018

Accepted: 27.02.2019

Published: 01.04.2019

Copyright: © 2019 This is an open access article under the terms of the CC-BY 4.0, which permits unrestricted use, distribution, and reproduction in any medium, provided the original author and source are credited.

INTRODUCTION

To guarantee a sustainable use of resources and protection of environment, it is of substantial significance to follow and optimize lightweight solutions in mobility, in particular in automotive industry. However, these solutions have to follow other requirements, like maximum driving range or safety features. Lightweight optimization can be



achieved by the progressive development of microstructure-based materials design to increase the component's load limits and hence, to follow the concept of downsizing. Cast aluminum alloys as an often chosen material in highly-stressed parts of the automobile drivetrain provide an outstanding strength to weight ratios due to their low density and the strengthening potential of some alloys. Previous studies had shown that under cyclic loading the fatigue properties are defined by microstructural characteristics, like secondary dendrite arm spacing (SDAS) [1-4], porosity [5-8] and the morphology of the eutectic silicon [9-10]. These parameters are strongly influenced by the cooling rates during the casting [11], especially, when the components are of high volume and showing a variation in wall thickness. Some of these defects are of interacting nature, i.e., porosities are initiated if the solidification front is hindered by plate-shaped intermetallic precipitates, like α - or β -AlFeSi [11]. Since casting defects, like pores, geometrically complex intermetallic phases or plate-shaped eutectic silicon, are more or less in general present in industrially produced castings, it is essential to analyze the correlations between cooling processes, microstructures and fatigue properties, to reduce the high safety factors resulting from the conservative design guidelines, which are used in current structural integrity concepts. It is the aim of the present work to describe the dominating mechanisms of fatigue damage in aluminum castings, with a focus on crack initiation and microstructure-controlled crack propagation. Specimens were taken from in-series engine blocks (AlSi8Cu3) and cylinder heads (AlSi7Cu0.5Mg) and tested under uniaxial cyclic mechanical load in regimes of high-cycle-fatigue (HCF, up to 10^7 cycles) and very-high-cycle-fatigue (VHCF, between 10^7 and 10^9 cycles) and under pure bending. The resulting scientific findings serve as input data to adjust and to extend an existing short crack model based on the boundary element method (BEM), which is described in detail, e.g., in [12-13], and which is based on the concept that fatigue crack propagation is hindered by microstructural barriers (cf. Navarro and de los Rios [14] and Hall-Petch relation [15]).

EXPERIMENTAL

The experiments in this work were performed using two conventional hypoeutectic cast aluminum alloys, AlSi8Cu3 representing a secondary metallurgy alloy used for engine blocks, and AlSi7Cu0.5Mg, representing a primary metallurgy alloy used for cylinder heads. Specimens were extracted according to the sketch in Fig. 1, from two different locations of the in-series castings (T6 heat treated) with a maximum difference in the cooling rate and SDAS.

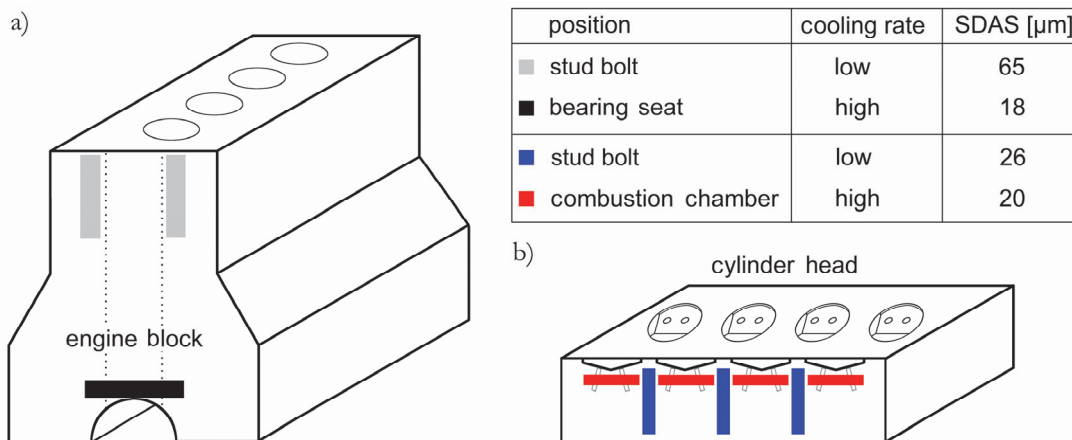


Figure 1: Positions of specimen extraction for a) the engine block (AlSi8Cu3) and b) the cylinder head (AlSi7Cu0.5Mg) with the respective relative cooling rates and SDAS values.

The high gradient in the cooling rate and thus, the respective difference in the appearance of the microstructure for the example of the engine block is forced by the use of chill castings. Here, chill elements are leading to a significantly faster solidification rate due to a higher gradient in temperature and, as compared to a non-cooled part in the casting, to a finer microstructure as it can be seen in Fig. 2. To show the dependency of the SDAS λ_2 from cooling rate and the solidification time t_s , Eqn. 1 can be taken from [16]. Here the variable k is depending on the aluminum cast alloy system. For the analyzed alloys $k = 11$ to $12 \mu\text{m}/\text{s}^{1/3}$.

$$\lambda_2 = k \cdot \sqrt[3]{t_s} \quad (1)$$

According to the faster solidification the eutectic is located more likely in the interdendritic regions than in big eutectic cells. Further the time for growth of pre eutectic intermetallic phases in case of the engine blocks bearing seat (see Fig. 2b) is significantly reduced. This leads to a decrease of their amount of different species, their size and geometrical complexity [11].

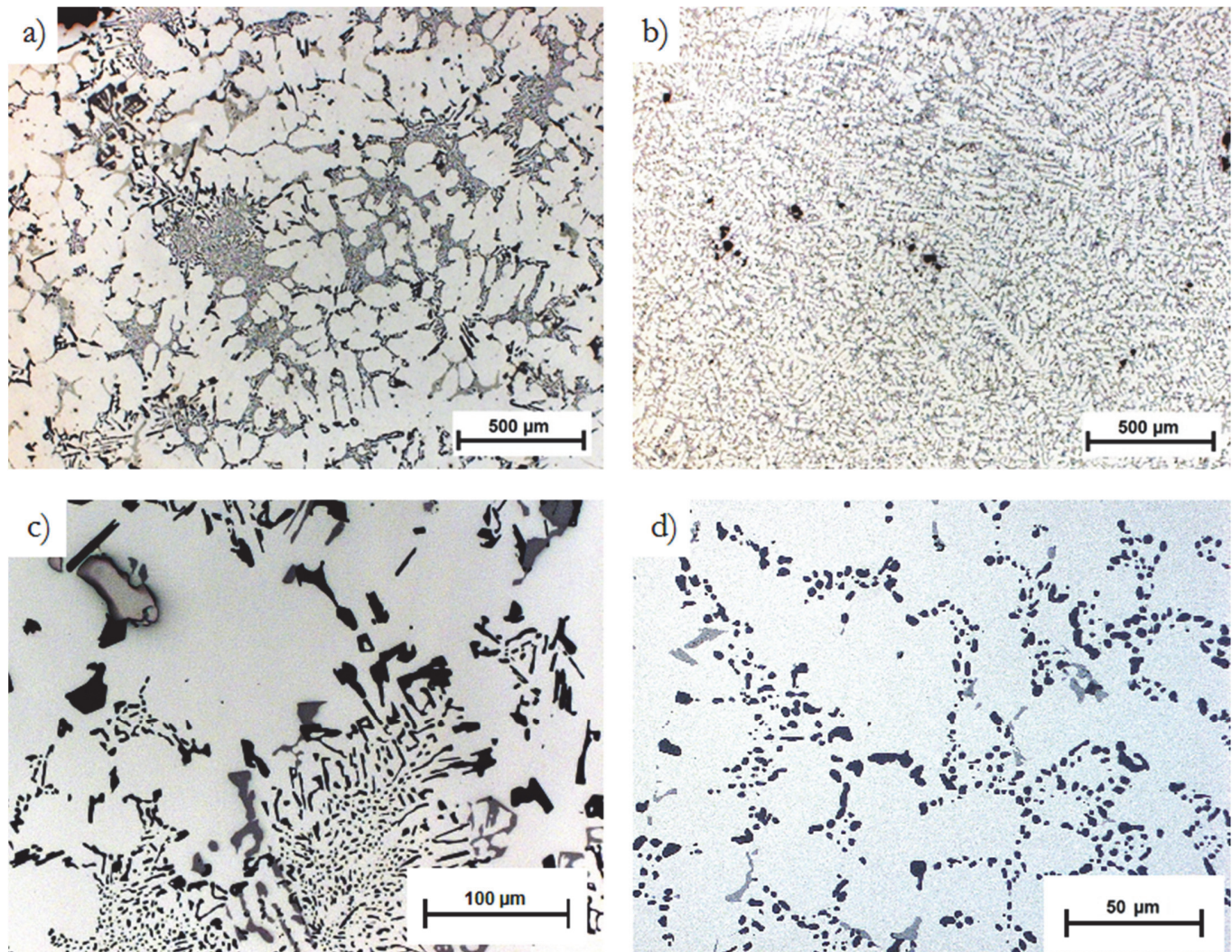


Figure 2: Overview micrographs (same magnification) of the cooling rate dependent microstructure taken from engine blocks a) stud bolt (low cooling rate) and b) bearing seat (high cooling rate). A detailed view to the microstructural components like eutectic Si and intermetallic particles are given by c) for the stud bolt and d) for the bearing seat.

In direct comparison of the microstructures, as shown in Fig. 2, one can see a significant difference in the occurrence of the cast aluminum characteristics, like the SDAS and the morphology of the eutectic Si. The SDAS was analyzed by the use of the BDG method P220 [16]. For a stable statistical value of this microstructural component a minimum of three evaluable micrographs with a minimum of ten well-defined dendrites in each case were analyzed. Furthermore, the difference in shape, size and modality of the eutectic Si is visible (see Fig. 2c and 2d). While the eutectic Si particles in the stud bolt appears bimodal (in some regions it occurs small and round; in others its morphology is bigger and needle- or plate-shaped), in the bearing seat the eutectic Si appearance is consistently fine and round. This characteristic was evaluated with a shape parameter that compares the shape of a single eutectic Si particle with a circle, where a perfect circle corresponds to the value 1 and a one-dimensional line to the value 0. These parameters for each alloy and investigated casting part is given in Tab. 1.



alloy	position	relative cooling rate	SDAS [μm]	shape factor [-]
AlSi8Cu3 engine block	stud bolt	lowest	65 ± 9.4	0.56
	bearing seat	highest	18 ± 2.5	0.77
AlSi7Cu0.5Mg cylinder Head	stud bolt	lowest	26 ± 2.4	0.85
	combustion chamber	highest	20 ± 1.8	0.83

Table 1: Measured microstructural characteristics, i.e., SDAS and shape factor of the eutectic Si particles for all analyzed alloys and regions of different cooling rates.

The uniaxial cyclic mechanical experiments were carried out using an ultrasonic resonance testing machine from BOKU Vienna ($f = 20$ kHz) for the HCF and VHCF regime. For crack propagation and ΔK threshold tests under pure bending a resonance testing machine Rumul Cracktronic ($f = 100$ Hz) was used. Close-ups of the experimental setups and the used specimen geometries are shown in Fig. 3.

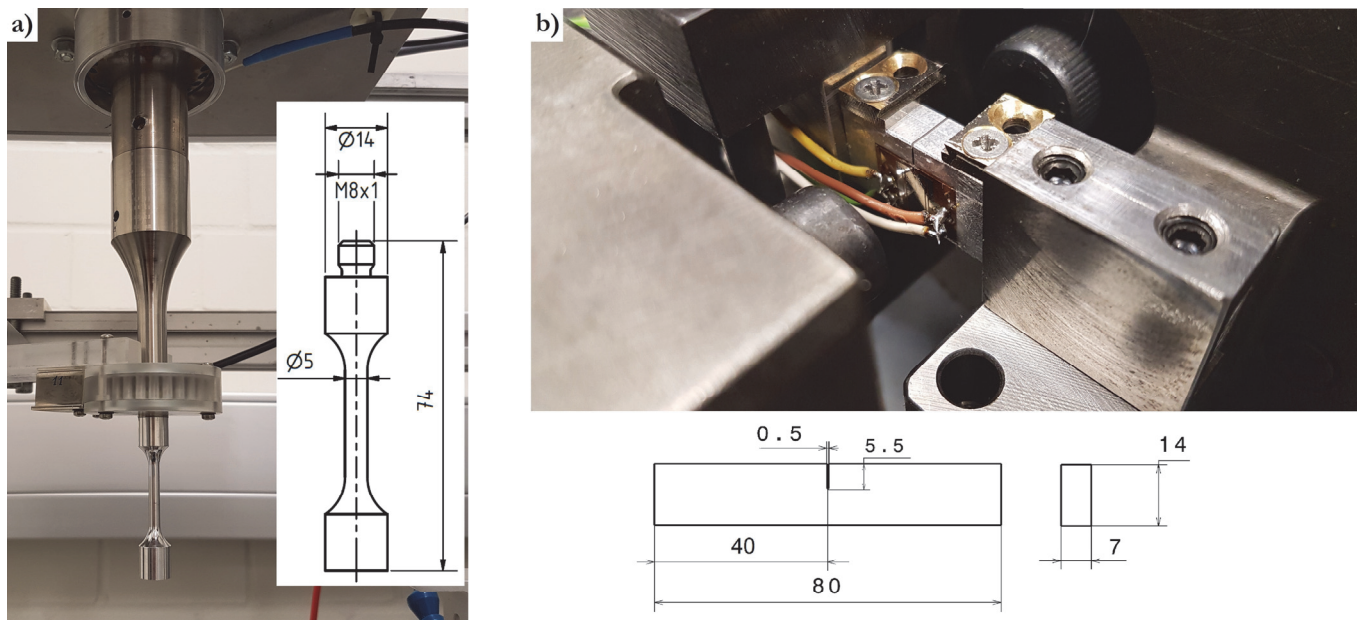


Figure 3: Close-up of the experimental setups and the respective specimen geometries; a) uniaxial fatigue testing in the ultrasonic resonance testing machine; b) single edge notch bend specimen (SENB) with crack gage attached in the resonance bending system Cracktronic.

All uniaxial cyclic mechanical tests were performed with a stress ratio of $R = -1$. As abort criterion for these experiments a maximal decrease in resonance frequency of $\Delta f = -2\%$ (fail) or a maximum number of cycles of $N = 10^9$ cycles (run through) was defined. To avoid specimen heating during high-frequency testing, air cooling and a pulse-pause mode was applied. Therefore, the specimens were loaded for 200 ms followed by a pause of 800 ms. To obtain statistically confirmed values for the fatigue limit, the experimental series follow the step method of Hück [17] assuming a fatigue limit criterion of $N = 10^7$ cycles.

During the crack-propagation tests, the crack length was measured by means of indirect alternating-current-potential-drop method (ACPD) on SENB specimens. For this purpose crack gages were attached to the surface, positioned below the notch of the specimens (maximal measurable crack length $a_{max} = 5$ mm). The threshold value of the stress intensity factor (SIF) range for technical crack propagation $\Delta K_{I,th}$ is measured during a load shedding procedure. After establishing an initial pre crack with a length of $a_{pre} = 1.3$ mm by a stepwise reduction of the bending moment, the threshold test starts immediately with a 10 % higher load level. The SIF range ΔK_I is calculated as provided in Eqn. 2 with the bending stress range $\Delta \sigma_b$, the total crack length a_{tot} , and the geometry factor $Y(a_{tot})$ for SENB specimens (cf. [18]). According to Paris and Erdogan [19-20], the crack-propagation rate da/dN as a function of SIF range ΔK_I can be calculated according to Eqn. 3, which is known as Paris law.

$$\Delta K_I = \Delta \sigma_b \cdot \sqrt{\pi \cdot a_{tot}} \cdot Y(a_{tot}) \quad (2)$$

$$\frac{da}{dN}(\Delta K) = C \cdot \Delta K^m \quad (3)$$

According to ASTM E 647 [21] the threshold value $\Delta K_{I,th}$ is calculable if there are a minimum of five measurement points for $10^{-10} \text{ m/cycle} < da/dN < 10^{-9} \text{ m/cycle}$. For this data points the best-fit line function for ΔK_I vs. da/dN has to be determined and further to be extrapolated to $da/dN = 10^{-10} \text{ m/cycle}$. The respective SIF range ΔK_I then represents the threshold $\Delta K_{I,th}$. To obtain the factor C and the exponent m of the Paris law, the bending moment was kept constant. Due to the progressing crack growth, the SIF and accordingly, the crack propagation rate increases until the maximum crack length a_{max} is reached. The SENB specimens were analyzed post-testing by means of light microscopy and a high-resolution scanning electron microscope (SEM), Zeiss Auriga FEG, equipped with EBSD (electron back-scatter diffraction) to correlate the crack paths to microstructural characteristics and crystallographic orientations.

RESULTS AND DISCUSSION

The uniaxial cyclic testing experiments, referring to [17], reveal a significant difference in the fatigue limit for the specimens with different cooling rates during casting. Results can be found in Tab. 2 linked with the respective SDAS, porosity area fraction and the average pore diameter d_p .

alloy	position	SDAS [μm]	fatigue limit σ_f [MPa]	porosity area fraction [%]	av. pore diameter d_p [μm]
AlSi8Cu3	stud bolt	65 ± 9.4	68 ± 1	1.81	47.7
engine block	bearing seat	18 ± 2.5	114 ± 23	0.12	9.3
AlSi7Cu0.5Mg	stud bolt	26 ± 2.4	≈ 90	0.17	8.5
cylinder Head	combustion chamber	20 ± 1.8	122 ± 22	0.11	5.5

Table 2: Fatigue limits σ_f , fraction of porosity and average pore diameter d_p for both cast alloys and the respective extraction position for in-series castings linked to the measured SDAS.

However, for high and low cooling rates the specimens contain different fractions of porosities and in varying shape and size, which were found to be the major origin and position of crack initiation. A more detailed study of the influence of porosity on fatigue with respect to their extreme values, distribution and shape is given in [22]. In the present work porosity in varying occurrence is first of all considered as point of locally raised stress intensity and related to that, origin of fatigue crack initiation. In this context porosity analysis showed that pores are much larger, more complex in geometry (due to shrinkage) and tending to higher fractions if the cooling rates are low. In such cases (engine block stud bolt), crack-provoking pores are of higher diameters and located straight below or at the surface. For the other specimen series of higher cooling rates (engine block → bearing seats; cylinder head → combustion chamber), the cracks initiate at surface-near porosity accumulations. Both cases of crack initiation are shown in the fracture surface micrographs in Fig. 4.

Even though, the total porosity fraction is significantly lower and the pore diameter is smaller for the finer microstructure, as shown in Fig. 4b, the occurrence of a porosity accumulation in near-surface regions leads to a locally high stress intensity, which is fatal in the HCF and the VHCF regime. It was found during testing that, e.g., two specimens extracted from the same engine block batch and fatigued at the same stress amplitude tended to completely different numbers of cycles to fail. The specimen shown in the micrograph Fig. 4b failed after $1.8 \cdot 10^6$ cycles under a stress amplitude of 120 MPa due to a fast crack initiation at the subsurface pore accumulation. A second specimen was fatigued up to $3.9 \cdot 10^8$ cycles under the same conditions and no significant pores were found at the crack initiation site. However, a large facet region can be observed at the fracture surface, which cuts the specimen surface so the crack initiation and the crack propagation are shear-stress controlled and dominated by crystallographic mechanisms in absence of a critical state of porosity. The described fracture surface is shown in Fig. 5. Compared to the first case, the crack initiation and micro crack propagation took a high amount of cycles and the specimen showed a significant higher endurance. Such inhomogeneities in the occurrence and



distribution of pores like in the described example are leading to the shown scatterings during the uniaxial cyclic tests in the HCF and VHCF regime (see Tab. 2) and big differences in the appearance of the fracture surface. If there are pores of higher diameter or of critical accumulated states the fracture surface shows striations and is oriented orthogonal to the loading axis. However, in the absence of porosity cracks are initiating and propagating shear-stress controlled on highly loaded slip planes (see Fig. 5).

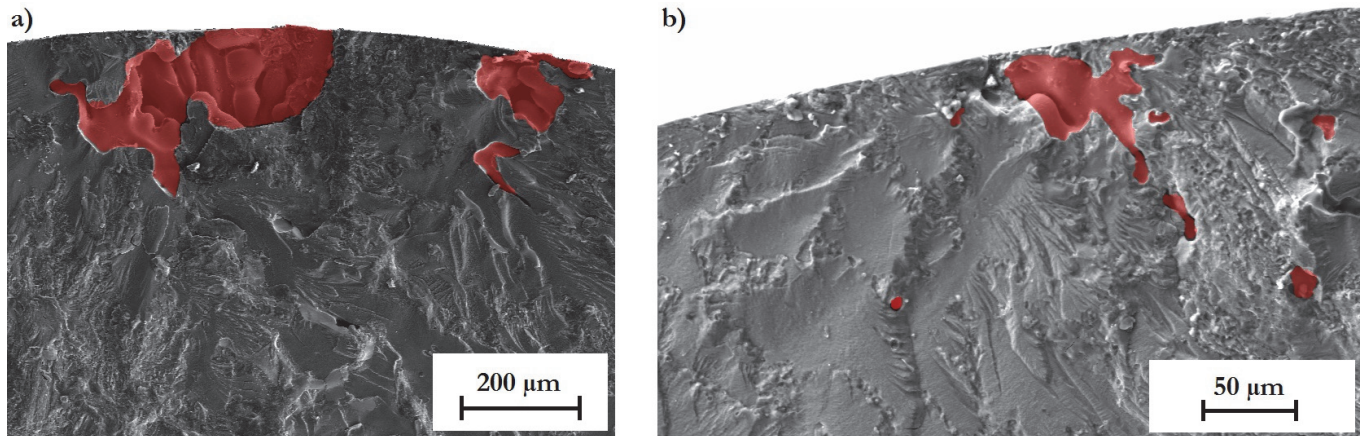


Figure 4: Fracture surface micrographs of typical crack-initiating pores (red surroundings) for a) low cooling rate, high SDAS ($65 \mu\text{m}$), pores of bigger diameter, and b) high cooling rate, low SDAS ($18 \mu\text{m}$), small and less pores but accumulated and surface-near.

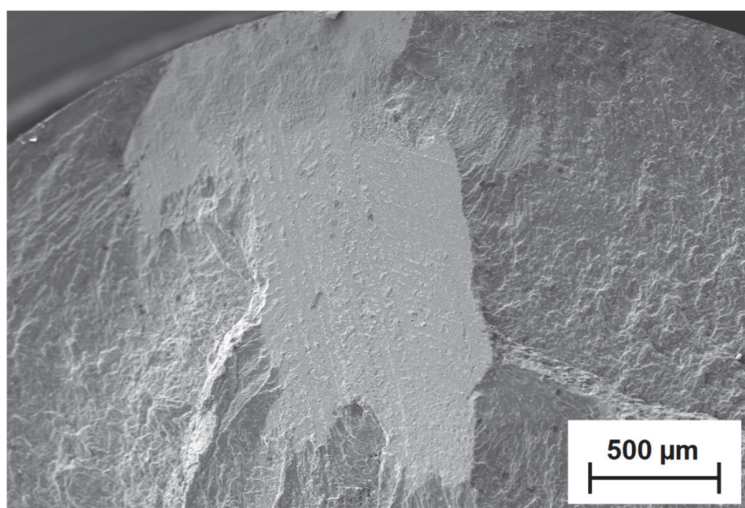


Figure 5: Fracture surface micrograph of a specimen from engine blocks bearing seat after $N_f = 3.9 \cdot 10^8$ cycles ($\sigma_a = 120 \text{ MPa}$). A large faceted area ranging from specimen's surface to the center. Dendritic as well as interdendritic regions are observable at the facet fracture surface.

For the shown mechanism of microstructural crack propagation in the first part of HCF and VHCF damaging usually the grain size is an influencing microstructure parameter. This is explained by the reduction in the mean free path of dislocation movement, proportional to the grain diameter and concluded in the Hall-Petch relation. In this context grain boundaries act as barriers against dislocation slip and are more frequently present for lower grain sizes. With respect to the general appearance of hypoeutectic aluminum cast alloy microstructures (dendritic) the use of the SDAS value instead of the grain size makes more sense. The fact that slip planes are crossing the interdendritic eutectic regions (cf. Fig. 5) allows them to act as barriers, too. This kind of interaction with the crack propagation behavior will be show in more detail in the section of crack propagation experiments. Thus, as for example observable for the cylinder head alloy AlSi7Cu0.5Mg (small differences in porosity occurrence but in SDAS; cf. Tab. 2) the fatigue limit is increased for lower SDAS.

The results of the crack-propagation experiments with regard to the threshold values and the Paris law parameters are summarized in Tab. 3 based on the data represented in the crack propagation vs. SIF range in Fig. 6a further below.

alloy	position	SDAS [μm]	threshold SIF range $\Delta K_{I,th}$ [MPa · m ^{0.5}]	constant C [10 ⁻¹¹]	exponent m
AlSi8Cu3	stud bolt	65 ± 9.4	7.0	0.88	2.9
engine block	bearing seat	18 ± 2.5	4.4	1.06	2.8
AlSi7Cu0.5Mg	stud bolt	26 ± 2.4	7.55	0.58	2.9
cylinder head	combustion chamber	20 ± 1.8	8.66	0.04	2.9

Table 3: Results from crack propagation tests for all cast aluminum alloys and extraction positions of this study.

The experiments show that the material with the lowest SDAS value exhibits the weakest resistance against technical crack initiation (for crack lengths which exceeds the microstructural scale), i.e., the determined threshold value $\Delta K_{I,th}$ for the engine blocks bearing seat position is the lowest one in this study (see Tab. 3). Usually, a significant drop in the crack propagation rate da/dN is observable after it reaches values below 10^{-9} m/cycle. However, in the case of the engine block bearing seat there is a quite mild decrease that can be seen in Fig. 6a and will be discussed more detailed further below.

The threshold SIF range for crack-propagation and the fatigue limit data were linked to create a crack threshold diagram according to Kitagawa and Takahashi [23], including the modification according to El Haddad [24] using the Eqns. 4 and 5 with $\Delta\sigma_{th}$ being the threshold stress amplitude for onset of stable technical crack advance, a_0 as the technical threshold crack/defect length and a being varying defect size. As Eqn. 5 shows a_0 is depending on the threshold value $\Delta K_{I,th}$ and thus underneath this crack length no technical crack propagation will occur if the stress amplitude did not exceed the fatigue limit σ_f . However this means not that there will be no crack propagation at all, microstructural dominated short crack growth is possible at very low crack propagation rates da/dN . This issue will be discussed further below. Fig. 6 is showing the crack propagation rate da/dN versus the SIF range ΔK_I and the respective Kitagawa-Takahashi diagram for the example of the engine block alloy AlSi8Cu3 to demonstrate the difference in influence of the SDAS on the fatigue limit σ_f and the crack propagation threshold $\Delta K_{I,th}$, respectively.

$$\Delta\sigma_{th} = \frac{\Delta K_{I,th}}{\sqrt{\pi \cdot (a + a_0)}} \quad (4)$$

$$a_0 = \frac{1}{\pi} \cdot \left(\frac{\Delta K_{I,th}}{\Delta\sigma_f} \right)^2 \quad (5)$$

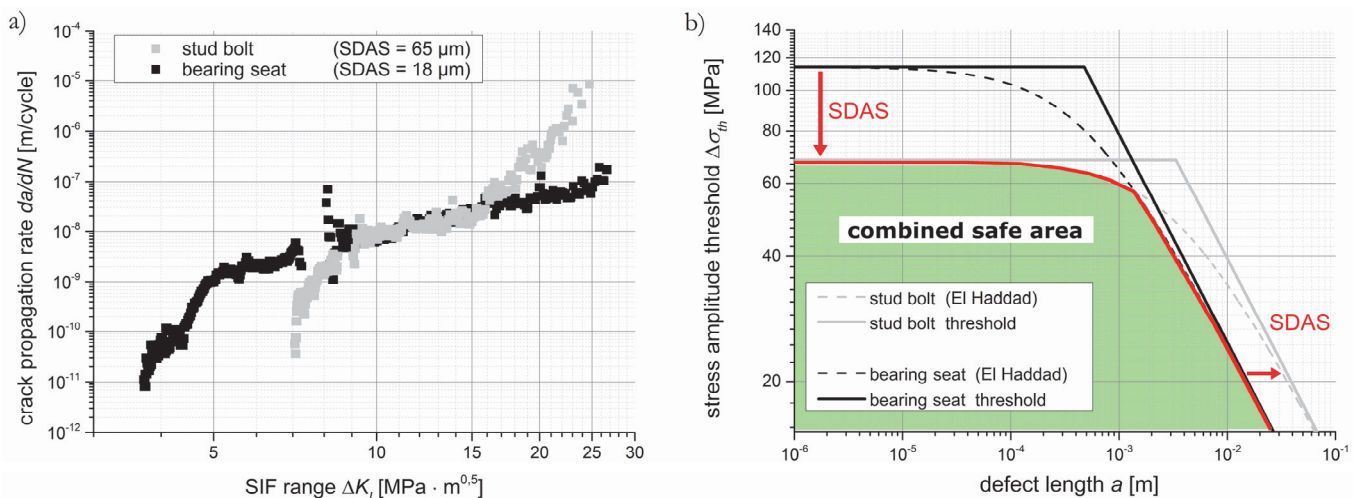


Figure 6: Fatigue crack propagation in the engine block alloy AlSi8Cu3; a) crack propagation rate da/dN vs. SIF range ΔK_I (stress ratio $R = -1$); b) Kitagawa-Takahashi diagram with the El Haddad modification and marked SDAS influence. Furthermore, a combined safe area for both microstructural appearances from the same casting is highlighted (green area).

The most important advantage of the Kitagawa-Takahashi diagram is to get a quick but reliable overview if a given combination of defect size and loading amplitude is critical with respect to a desired fatigue limit number of cycles. A test



of its validity is easily possible if specimens which fail below the fatigue limit or run out ($N \geq 10^7$) in the near of it will be analyzed with respect to the dimension of either their crack initiating defect or their most critical but not propagating defect. In this context some corresponding data points (applied cyclic amplitude σ_a , initial defect length and SDAS) of this study and further results of an alloy with quite similar chemical composition and microstructure parameters according to the SDAS, taken from literature can be found in Tab. 4 and are implemented in the Kitagawa-Takahashi diagram of Fig. 7. The inserted points from literature are well summarized from different studies by Wang et al. [25]. Here every point is related to a fatigue limit σ_f , a SDAS value and a pore area, measured at the fracture surfaces. Analogue to this the defect size in this study (crack initiating pore for failure or biggest pore for run through events) was measured at the fracture surface after testing. In case of the run out events the specimens were cracked later by monotonic increasing tensile stress. All defect lengths a are given as maximal diameter of the crack initiating or biggest pores for values of the present work or as calculated diameter of an equivalent circular defect according to the pore area values of [25].

alloy	study	SDAS [μm]	stress amplitude σ_a / fatigue limit σ_f [MPa]	failure before $N = 10^7$ cycles	defect length a [μm]
AlSi8Cu3 stud bolt	this study	65	68	yes	1103
			66	no	271
		18	110	yes	103
			110	no	19
AlSi6Cu3.5 (A319)	Wang et al. [25]	66	66	no	374
			62	no	451
		20	112	no	(quasi defect free)
			97	no	220

Table 4: Combined data points of applied cyclic loading and defect lengths (maximal pore diameter measured at fracture surfaces) from uniaxial cyclic loading tests of this study for the engine block alloy AlSi8Cu3. Further, similar results from Wang et al. [25] are given to test the validity of the created Kitagawa-Takahashi diagram.

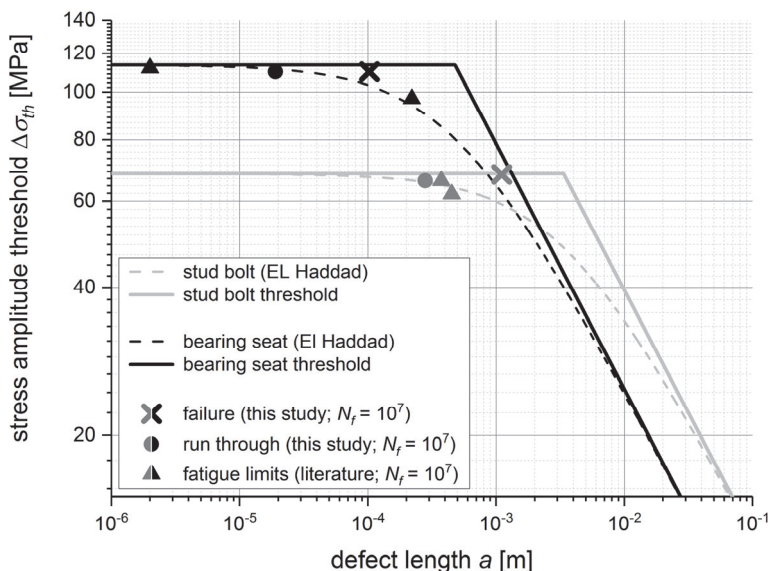


Figure 7: The Kitagawa-Takahashi diagrams for the engine blocks stud bolt (grey; SDAS = 65 μm) and bearing seat (black; SDAS = 18 μm) extended by the data points shown in Tab. 4.

It is visible that the points of run throughs are on the left side (safe area) of the respective El Haddad curve according to the materials SDAS. Further, experiments which fail although the stress amplitude is below the fatigue limit are positioned at the right side of the El Haddad-modified threshold (failure area). The fatigue limits σ_f ($N_f = 10^7$) from literature (cf. Tab. 4) are laying on or near the El Haddad threshold curve what underline its validity.

The more compact material taken from bearing seats with lower SDAS shows a better resistance against crack propagation for higher SIF ranges (cf. Fig. 6a); however, the threshold for technical short crack propagation $\Delta K_{I,th}$ is obviously lower than it was observed in the case of higher SDAS (stud bolt position, coarse microstructure). It should be mentioned that on the other hand the fatigue limit (horizontal lines in Fig. 6b) is significantly higher for lower SDAS. These results are analogues to the Hall-Petch-type relationships as found, e.g., in the case of steels [15, 26-27]. In the present case, the governing microstructural parameter is the SDAS instead of the alloy grain size as mentioned and explained further above. The local variation in crack propagation paths and mechanisms due to different cooling rate dependent on SDAS is shown in Fig. 8.

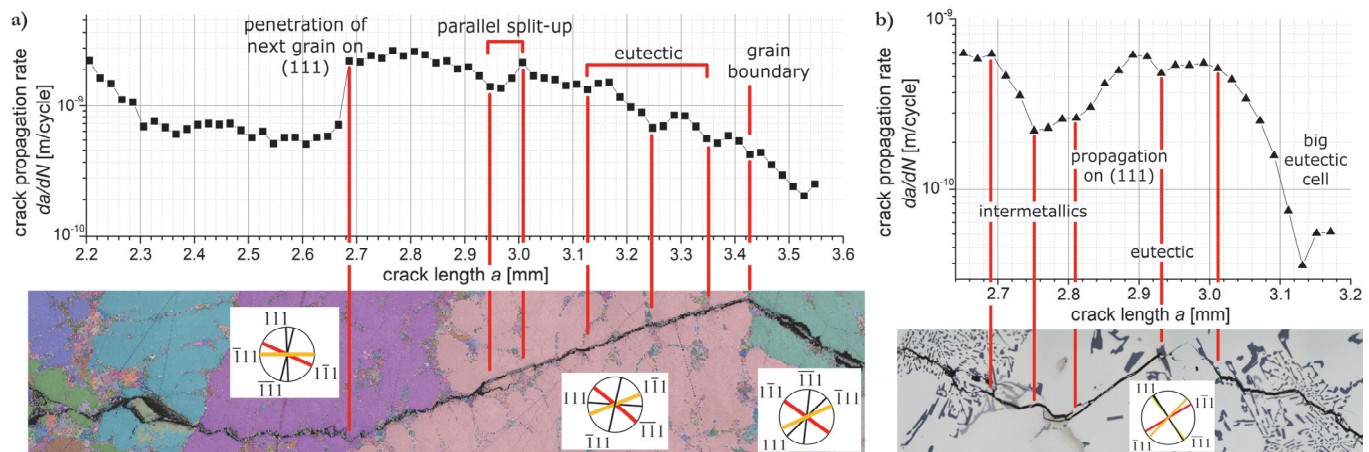


Figure 8: Crack propagation rate vs. crack length position for two SENB specimens of two different SDAS near the SIF range threshold (ΔK_I between 7.5 and 8.5 MPa · m^{0.5}) linked to a) an EBSD-micrograph of the cylinder head stud bolt (SDAS = 26 μm); b) a light microscopy micrograph of the engine block stud bolt (SDAS = 65 μm).

Fig. 8a shows that the crack propagation rate after having reached the SIF threshold was increased after penetration of the next grain by operating a (111) slip plane with a high Schmid factor of $M_S = 0.46$. Furthermore, it was observed that the crack was slowed down by interdendritic eutectic areas and parallel branching of the crack front. At the grain boundary at a crack length of $a = 3.42$ mm (Fig. 8a) no significant drop in the crack propagation rate was observed, since further propagation also follows a (111) slip plane with a high Schmid factor of $M_S = 0.46$. Fig. 8b represents the material with the lowest cooling rate and correspondingly high SDAS (engine block stud bolt position). Here, the crack follows critically loaded (111) slip planes (between 2.8 mm < a < 2.9 mm). However, large microstructural barriers like intermetallic phases or eutectic cells decrease the crack propagation rate significantly.

It is subject of current work to implement the microstructure in a short crack simulation concept based on the boundary element method, which is based on the concept of microstructural barriers. For the purpose to obtaining a systematic variation in SDAS, wedge-shaped specimens with step-wise decreasing thickness and hence, stepwise decreasing SDAS (due to increasing cooling rates) have been cast and are currently object of metallographic and mechanical investigation. During further fatigue experiments a shallow notch will be added to the specimens that allow an in-situ observation by means of thermography and optical microscopy. Prior to these testing, the shallow notch areas will be investigated by means of EBSD to correlate the crack initiation and propagation paths with the crystallographic orientation. With the results of this experiments the material model needed for the short crack simulation concept will be developed.

CONCLUSIONS

Fatigue and fatigue crack propagation experiments on two different in-series cast aluminum alloys revealed significant effects of the cooling-rate-dependent secondary dendrite arms spacing (SDAS). Lower SDAS are coincident with a higher fatigue limit σ_f but the resistance against crack propagation at low SIF ranges and the threshold value $\Delta K_{I,th}$ for technical crack initiation is noticeably reduced. Crack initiation in the uniaxial cyclic loading tests was shown to occur at large pores (low cooling rate) or at porosity accumulations (high cooling rate). Especially the heterogenous distribution of such micro porosity leads to a strong scattering in fatigue testing and to a variation in crack initiation, propagation and the



preferred crack paths. In absence of critical porosity, cracks are initiating and propagating shear-stress controlled on highly loaded slip planes.

The Kitagawa-Takahashi diagrams which were derived from the uniaxial cyclic loading and crack propagation tests are good tools to show and understand why the heterogenic occurrence of the porosity leads to big scattering in the fatigue experiments. Furthermore, their validity was shown by the implementation of different examples of fatigue limits from literature for the hypoeutectic aluminum cast alloy AlSi6Cu3.5 which deals with a similar chemical composition and SDAS values.

In the experiments under pure bending on single edge notch bend specimens (SENB) cracks are propagating along (111) slip planes at lower SIF ranges and are blocked by microstructural barriers, i.e., interdendritic eutectic regions or intermetallic phases. The size and the distance between these microstructure features is of a high importance for the fatigue resistance in terms of crack stopping and failure tolerance. Since the crack-blocking effect of the interdendritic areas seems to be similar to the one of the grain boundaries in polycrystalline alloys, the SDAS can be understood as an analogy to the grain size according to the Hall-Petch relationship.

ACKNOWLEDGEMENTS

The authors acknowledge the financial and technical support by the German Ministry of Education and Research (BMBF), by Deutsche Forschungsgemeinschaft (DFG), by Nemak Dillingen GmbH and RWP GmbH.

REFERENCES

- [1] Zhang, B., Poirier, D.R. and Chen, W. (1999). Microstructural Effects on High-Cycle Fatigue-Crack Initiation in A356.2 Casting Alloy, *Metall. Mater. Trans. A*, 30(10), pp. 2659-2666. DOI: 10.1007/s11661-999-0306-3.
- [2] Lados, D.A. and Apelian, D. (2004). Fatigue crack growth characteristics in cast Al-Si-Mg alloys - Part I. Effect of processing conditions and microstructure, *Mater. Sci. Eng. A*, 385(1-2), pp. 200-211. DOI: 10.1016/j.msea.2004.06.073
- [3] González, R., González, A., Talamantes-Silva, J., Valtierra, S., Mercado-Solís, R.D., Garza-Montes-de-Oca, N.F. and Colás R. (2013). Fatigue of an aluminium cast alloy used in the manufacture of automotive engine blocks, *Int. J. Fatigue*, 54, pp. 118-126. DOI: 10.1016/j.ijfatigue.2013.03.018.
- [4] Houria, M.I., Nadot, Y., Fathallah, R., Roy, M. and Maijer, D.M. (2015). Influence of casting defect and SDAS on the multiaxial fatigue behavior of A356-T6 alloy including mean stress effect, *I. J. Fatigue*, 80, pp. 90-102. DOI: 10.1016/j.ijfatigue.2015.05.012.
- [5] Ceschini, L., Morri, A. and Sambogna, G. (2008). The effect of hot isostatic pressing on the fatigue behavior of sand-cast A356-T6 and A204-T6 aluminum alloys, *J. Mater. Process. Technol.*, 204(1-3), pp. 231-238. DOI: 10.1016/j.jmatprotec.2007.11.067.
- [6] McDowell, D.L., Gall, K., Horstemeyer, M.F. and Fan, J. (2003). Microstructure-based fatigue modeling of cast A356-T6 alloy, *Eng. Fract. Mech.*, 70(1), pp. 49-80. DOI: 10.1016/S0013-7944(02)00021-8.
- [7] Yi, J.Z., Gao, Y.X., Lee, P.D., Flower, H.M. and Lindley, T.C. (2003). Scatter in fatigue life due to effects of porosity in cast A356-T6 aluminum-silicon alloys, *Metall. Mater. Trans. A*, 34A(9), pp. 1879-1890. DOI: 10.1007/s11661-003-0153-6.
- [8] Ben Ahmed, A., Nasr, A., Bahloul, A. and Fathallah, R. (2017). The impact of defect morphology, defect size, and SDAS on the HCF response of A356-T6 alloy, *Int. J. Adv. Manuf. Tech.*, 92(1-4), pp. 1113-1125. DOI: 10.1007/s00170-017-0192-6.
- [9] Siegfanz, S., Giertler, A., Michels, W. and Krupp, U. (2013). Influence of the microstructure on the fatigue damage behavior of the aluminium cast alloy AlSi7Mg0.3, *Mater. Sci. Eng. A*, 565, pp. 21-26. DOI: 10.1016/j.msea.2012.12.047
- [10] Gall, K., Yang, N., Horstemeyer, M., McDowell, D.L. and Fan, J.H. (1999). The Debonding and Fracture of Si Particles during the Fatigue of a Cast Al-Si Alloy, *Metall. Mater. Trans. A*, 30(12), pp. 3079-3088. DOI: 10.1007/s11661-999-0218-2.
- [11] Lu, L. and Dahle, A.K. (2005). Iron-Rich Intermetallic Phases and Their Role in Casting Defect Formation in Hypoeutectic Al-Si Alloys, *Metall. Mater. Trans. A*, 36(13), pp. 819-835. DOI: 10.1007/s11661-005-1012-4.



- [12] Künkler, B. (2007). Mechanismenorientierte Lebensdauervorhersage unter Berücksichtigung der Mikrostruktur - Modellentwicklung, Verifikation und Anwendung, Dissertation, VDI-Verlag, Faculty of Mechanical Engineering, University of Siegen.
- [13] Krupp, U. (2007). Fatigue Crack Propagation in Metals and Alloys, Wiley VCH, Weinheim.
DOI: 10.1002/9783527610686.
- [14] Navarro, A. and de los Rios, E.R. (1988). Short and Long Fatigue Crack Growth: A Unified Model, *Philos. Mag. A*, 57(1), pp. 15-36. DOI: 10.1080/01418618808204496.
- [15] Hall, E.O. (1951). The Deformation and Ageing of Mild Steel: III Discussion of Results, *Proc. Phys. Soc. B*, 64(9), pp. 747-753. DOI: 10.1088/0370-1301/64/9/303.
- [16] Fachausschuss „Leichtmetallguss“ im BDG (2011). P220 - Bestimmung des Dendritenarmabstandes für Gussstücke aus Aluminium-Gusslegierungen, BDG-Richtlinie, Düsseldorf. Available at: https://www.bdguss.de/fileadmin/content_bdguss/Der_BDG/Richtlinien/P_220.pdf.
- [17] Hück, M. (1983). Ein verbessertes Verfahren für die Auswertung von Treppenstufenversuchen, *Mater. Sci. Eng. Technol.*, 14(12), pp. 406-417. DOI: 10.1002/mawe.19830141207.
- [18] Gross, D. and Seelig, T. (2011). Bruchmechanik, fifth ed., Springer, Berlin. DOI: 10.1007/978-3-642-10196-0.
- [19] Paris, P.C., Gomez, M.P. and Anderson, W.E.A. (1961). Rational Analytic Theory of Fatigue, *The Trend in Engineering*, 13 (1961) 9-14.
- [20] Paris, P.C. and Erdogan, F.A. (1963). Critical Analysis of Crack Propagation Laws, *J. Basic Eng.*, 85(4), pp. 528-533. DOI: 10.1115/1.3656900.
- [21] ASTM International (2000). E 647 - Standard Test Method for Measurement of Fatigue Crack Growth Rates, West Conshohocken. DOI: 10.1520/E0647-15E01.
- [22] Tenkamp, J., Koch, A., Knorre, S., Krupp, U., Michels, W. and Walther, F. (2018). Defect-correlated fatigue assessment of A356-T6 aluminum cast alloy using computed tomography based Kitagawa-Takahashi diagrams, *Int. J. Fatigue*, 108, pp. 25-34. DOI: 10.1016/j.ijfatigue.2017.11.003.
- [23] Kitagawa, H. and Takahashi, S. (1976). Applicability of fracture mechanics to very small cracks, In ASM Proceedings of 2nd international conference on mechanical behavior of materials, Metalspark, Ohio, pp. 627-631.
- [24] El Haddad, M.H., Topper, T.H. and Smith, K.N. (1979). Prediction of non propagating cracks, *Eng. Fract. Mech.*, 11(3), pp. 573-584. DOI: 10.1016/0013-7944(79)90081-X.
- [25] Wang, Q.G., Davidson, C.J., Griffiths, J.R. and Crepeau P.N. (2006). Oxide Films, Pores and the Fatigue Lives of Cast Aluminum Alloys, *Metall. Mater. Trans. B*, 37(6), pp. 887-895. DOI: 10.1007/BF02735010.
- [26] Chapetti, M.D., Miyata, H., Tagawa, T., Miyata, T. and Fujioka, M. (2004). Fatigue strength of ultra-fine grained steels, *Mater. Sci. Eng. A*, 381(1-2), pp. 331-336. DOI: 10.1016/j.msea.2004.04.055.
- [27] Sadananda, K. and Vasudevan, A.K. (2003). Fatigue crack growth mechanisms in steels, *Int. J. Fatigue*, 25(9-11), pp. 899-914. DOI: 10.1016/S0142-1123(03)00128-2.